Electrothermal MEMS parallel plate rotation for single-imager stereoscopic endoscopes

Kyung-Won Jang,[1] Sung-Pyo Yang,[1] Seung-Hwan Baek,[2] Min-Suk Lee,[1] Hyeon-Cheol Park,[1] Yeong-Hyeon Seo,[1] Min H. Kim,[2] and Ki-Hun Jeong[1,*]

[1]*Korea Advanced Institute of Science and Technology (KAIST), Department of Bio and Brain Engineering, 291 Daehak-ro, Yuseong-gu, Daejeon 34141, South Korea*
[2]*Korea Advanced Institute of Science and Technology (KAIST), Department of Computer Science, 291 Daehak-ro, Yuseong-gu, Daejeon 34141, South Korea*
*kjeong@kaist.ac.kr

Abstract: This work reports electrothermal MEMS parallel plate-rotation (PPR) for a single-imager based stereoscopic endoscope. A thin optical plate was directly connected to an electrothermal MEMS microactuator with bimorph structures of thin silicon and aluminum layers. The fabricated MEMS PPR device precisely rotates an transparent optical plate up to 37° prior to an endoscopic camera and creates the binocular disparities, comparable to those from binocular cameras with a baseline distance over 100 μm. The anaglyph 3D images and disparity maps were successfully achieved by extracting the local binocular disparities from two optical images captured at the relative positions. The physical volume of MEMS PPR is well fit in 3.4 mm x 3.3 mm x 1 mm. This method provides a new direction for compact stereoscopic 3D endoscopic imaging systems.

References and links

1. M. F. Catalano, J. Van Dam, R. Bedford, R. M. Cothren, and M. V. Sivak, Jr., "Preliminary evaluation of the prototype stereoscopic endoscope: precise three-dimensional measurement system," Gastrointest. Endosc. **39**(1), 23–28 (1993).
2. N. Taffinder, S. G. T. Smith, J. Huber, R. C. G. Russell, and A. Darzi, "The effect of a second-generation 3D endoscope on the laparoscopic precision of novices and experienced surgeons," Surg. Endosc. **13**(11), 1087–1092 (1999).
3. D. Lee and I. Kweon, "A novel stereo camera system by a biprism," IEEE Trans. Robot. Autom. **16**(5), 528–541 (2000).
4. A. Yaron, M. Shechterman, and N. Horesh, "Blur spot limitations in distal endoscope sensors," Proc. SPIE **6055**, 605509 (2006).
5. L. Lipton, "Polarizing aperture stereoscopic cinema camera," Opt. Eng. **51**(7), 073202 (2012).
6. A. B. Greening and T. N. Mitchell, "Stereoscopic viewing system using a two dimensional lens system," U.S. Patent 5,828,487 (Oct 27, 1998).
7. W. Teoh and X. Zhang, "An inexpensive stereoscopic vision system for robots," in *Proceedings of IEEE International Conference on Robotics and Automation* (IEEE, 1984), pp. 186–189.
8. S. Y. Bae, R. Korniski, A. Ream, H. Shahinian, and H. M. Manohara, "New technique of three-dimensional imaging through a 3-mm single lens camera," Opt. Eng. **51**(2), 021106 (2012).
9. Y. Nishimoto and Y. Shirai, "A feature-based stereo model using small disparities," in *Proceedings of IEEE Conference on Computer Vision and Pattern Recognition* (IEEE, 1987), pp. 192–196.
10. C. Gao and N. Ahuja, "Single camera stereo using planar parallel plate," in *Proceedings of the 17th International Conference on Pattern Recognition* (IEEE, 2004), pp. 108–111.
11. W. Choi, V. Rubtsov, and C.-J. C. Kim, "Miniature flipping disk device for size measurement of objects through endoscope," J. Microelectromech. Syst. **21**(4), 926–933 (2012).
12. T. Shibata, J. Kim, D. M. Hoffman, and M. S. Banks, "The zone of comfort: Predicting visual discomfort with stereo displays," J. Vis. **11**(8), 11 (2011).
13. K. Jia, S. Pal, and H. Xie, "An electrothermal tip-tilt-piston micromirror based on folded dual S-shaped bimorphs," J. Microelectromech. Syst. **18**(5), 1004–1015 (2009).

14. A. Jain, A. Kopa, Y. Pan, G. K. Fedder, and H. Xie, "A two-axis electrothermal micromirror for endoscopic optical coherence tomography," IEEE J. Sel. Top. Quantum Eletron. **10**(3), 636–642 (2004).
15. W. Peng, "Optimization of thermally actuated bimorph cantilevers for maximum deflection," in *Proceedings of Nanotech 2003* (NSTI, 2003), pp. 376–379.
16. H. C. Park, C. Song, and K. H. Jeong, "Micromachined lens microstages for two-dimensional forward optical scanning," Opt. Express **18**(15), 16133–16138 (2010).
17. Y. J. Oh, J. J. Kim, and K. H. Jeong, "Biologically inspired biophotonic surfaces with self-antireflection," Small **10**(13), 2558–2563 (2014).
18. Q. Yang, "A Non-Local Cost Aggregation Method for Stereo Matching," in *Proceedings of IEEE Conference on Computer Vision and Pattern Recognition* (IEEE, 2012), pp. 1402–1409.
19. D. Comaniciu and P. Meer, "Mean shift: a robust approach toward feature space analysis," IEEE Trans. Pattern Anal. **24**(5), 603–619 (2002).
20. X. Mei, X. Sun, W. Dong, H. Wang, and X. Zhang, "Segment-Tree based Cost Aggregation for Stereo Matching," in *Proceedings of IEEE Conference on Computer Vision and Pattern Recognition* (IEEE, 2013), pp. 313–320.

1. Introduction

Three dimensional (3D) Stereoscopic imaging is rapidly utilized not only in machine vision but also in entertainment or even clinical applications. In particular, medical endoscope serves as an efficient tool for *in vivo* optical diagnosis or clinical surgery to investigate internal organs. The endoscopic operation mainly relys on visual feedback to control the position of an endoscopic distal end. However, conventional endoscopes still struggle with precise visual information due to a lack of the depth cue. Previous works have reported some clinical benefits for stereoscopic 3D imaging that can improve the volumetric perception [1] or the operational effectiveness with high precision during the endoscopic surgery [2]. Conventional 3D endoscopes with stereopsis still require the binocular configuration of two cameras with a baseline distance, which substantially increases the physical diameter of endoscopic distal end. Miniaturized stereoscopic imaging has been extensively implemented with a single imager based spatial or temporal division. The spatial division physically divides the active pixels of a single detector into two equal parts, which deliver the binocular disparities by using bi-prism [3], dual pupil imaging objective [4], or polarized filter [5]. This approach inherently decreases the imaging resolution due to the reduced number of active pixels. On the other hand, the temporal division alternately collects two different images with binocular disparities on a single detector over the time. Conventional temporal division techniques utilize split-apertures based on mechanical shutter [6], mirror [7], or complementary multi-band band-pass filter (CMBF) [8], which still reduces the field-of-view (FOV) by a half due to the physical split of an effective aperture. In contrast, a parallel-plate-rotation (PPR) technique can provide the full FOV with stereopsis by rotating an optically transparent plate prior to a single camera [9,10]. Depending on the rotational angle, this configuration slightly deflects the principal optical axis of a single camera and results in the virtual movement of the detector for binocular disparity. Recently, an electrostatic actuation for PPR has been demonstrated for the size measurement of an object [11]. However, the previous work still requires not only precise depth information but also stereo-matching algorithm for three dimensional stereoscopic imaging. In addition, it still requires the stereoscopic design for minimizing visual discomfort like visual fatigue or dizziness for practical use.

In this work, we report a single imager based electrothermal MEMS PPR device for 3D endoscopic imaging systems with stereopsis. Figure 1(a) shows a schematic illustration for electrothermal MEMS PPR device. The electrothermal microactuator comprises the bimorph structure of thin aluminum and silicon layers with thermal mismatch, which actuates the physical rotation of an anti-reflective optical plate. The working principle for MEMS PPR is also described in Fig. 1(b). A thin optical plate before a single endoscopic camera can be precisely rotated by using an electrothermal microactuator under low operating voltages. The dynamic rotation of an optical plate can create the binocular disparities from two optical images captured at different angles, comparable to those from conventional binocular cameras.
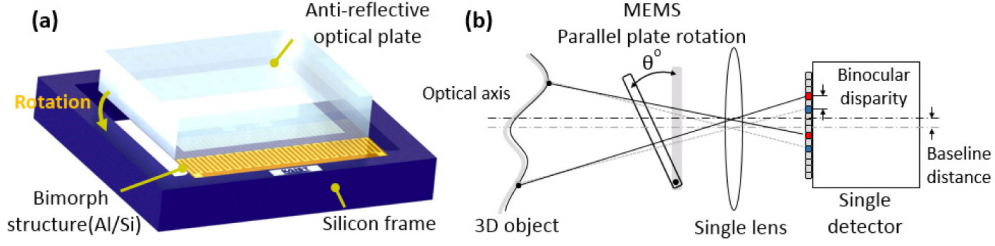
Fig. 1. MEMS Parallel Plate Rotation: (a) Schematic configuration of MEMS PPR device. The device comprises a transparent optical plate and an electrothermal MEMS actuator with bimorph structure. (b) Working principle of a single lens and single detector with electrothermal MEMS parallel-plate-rotation for stereoscopic endoscopy. A thin optical plate can be either dynamically or statically rotated with electrothermal actuation under low operating voltages. The plate rotation creates binocular disparities for depth cues, comparable to those from binocular cameras.

2. Stereoscopic vision and MEMS PPR design

The minimum depth-of-field (DOF) of conventional endoscopic cameras often starts from 3 mm and thus the baseline distance was set to be 100 μm, satisfying the 1/30 rule to yield the maximum allowable depth perception in comfortable viewing, i.e., a ratio of the baseline distance to the distance for a nearest object [12]. The baseline distance b for PPR can be expressed as follows:

$$b = t \sin \theta \left[1 - \sqrt{\frac{1 - \sin^2 \theta}{n^2 - \sin^2 \theta}} \right] \tag{1}$$

where t, θ, and n are the plate thickness, the incidence angle, and the refractive index of a rotating optical plate. Based on this calculation for $t = 500$ μm and $n = 1.51$, the rotation angle requires 30° to achieve the baseline distance of 100 μm. Such dynamic and large rotational angles can be obtained at a low operating voltage by using an electrothermal microactuator with bimorph structures of two adjacent materials with different coefficients of thermal expansion (CTE) [13,14]. The bimorph structures are substantially deflected during Joule heating due to the stress gradient induced by the mismatch in thermal expansion. The maximum rotation angle can also be expressed as:

$$\theta = \frac{ctw(1+t)^2}{c^2 t^4 w^2 + 4ct^3 w + 6ct^2 w + 4ctw + 1} \frac{3\Delta\alpha \cdot \Delta T \cdot L}{t_{Si} + t_{Al}} \tag{2}$$

where t_{Si} and t_{Al} are the thicknesses of bimorph layers, L is the bimorph length, $\Delta\alpha$ is the difference in CTE, ΔT is the temperature difference, $t = t_{Si}/t_{Al}$, $w = w_{Si}/w_{Al}$, and $c = (E_{Al}/(1-v_{Al}))/(E_{Si}/(1-v_{Si}))$, where w_{Si} and w_{Al} are the bimorph widths, E_{Si} and E_{Al} are the elastic moduli of bimorph layers, v_{Si} and v_{Al} are the Poisson's ratios [15], while the subscripts Si and Al signify silicon and aluminum, respectively. In this design, the bimorph structures consist of a 4 μm thick silicon membrane with meandered aluminum line pattern (9 μm in width, 1 μm in thickness), which provides the electrical resistance of 200 Ω and thermal mismatch during Joule heating. A 0.1 μm thick silicon nitride layer serves as an electrical insulator between the bimorph structures. All the static and dynamic analyses have been performed by using the finite element analysis. (FEA, COMSOL Multiphysics® ver. 4.3).

3. Device Fabrication

The device microfabrication was done by using a standard silicon-on-insulator (SOI) process at 6-inch wafer level. The cross-sectional views for the process flow are illustrated in Fig.

2(a). A 0.1μm thick silicon nitride layer was firstly deposited on a SOI-wafer (Top Si: Buried SiO$_2$: Bottom Si = 4 μm; 1.5 μm: 500 μm in thickness) by using low pressure chemical vapor deposition (LPCVD). A 1 μm thick aluminum lines were defined by using E-beam evaporation and lift-off. The silicon nitride layer was selectively etched by using reactive ion etching. The top silicon was defined as the plate holder by using deep reactive ion etching (DRIE). Next, the backside silicon was then defined by using DRIE after the front side passivation, where the individual chips were mechanically tethered on the wafer. After the removal of buried oxide, the individual chips were physically separated from the SOI wafer by applying the voltages for Joule heating and eventually packaged on the printed circuit board (PCB) after soldering electrical wires [16]. The plate holder exhibits an initial deflection of ~8° due to the residual stress of bimorph structures. The measured thin film stresses show 200 MPa in compression for the aluminum and 100 MPa in tension for the silicon nitride. Finally, a thick optical plate (borosilicate glass, t = 0.5 mm, n = 1.51) with anti-reflective structures in both side was permanently mounted on the plate holder by using a UV curable adhesive [17]. Figure 2(b) and 2(c) show the SEM and optical image of the microactuator before and after the integration of an optical plate. The overall physical volume of the MEMS PPR device with an optical plate is well fit within 3.4 mm (W) x 3.3 mm (L) x 1 mm (H).
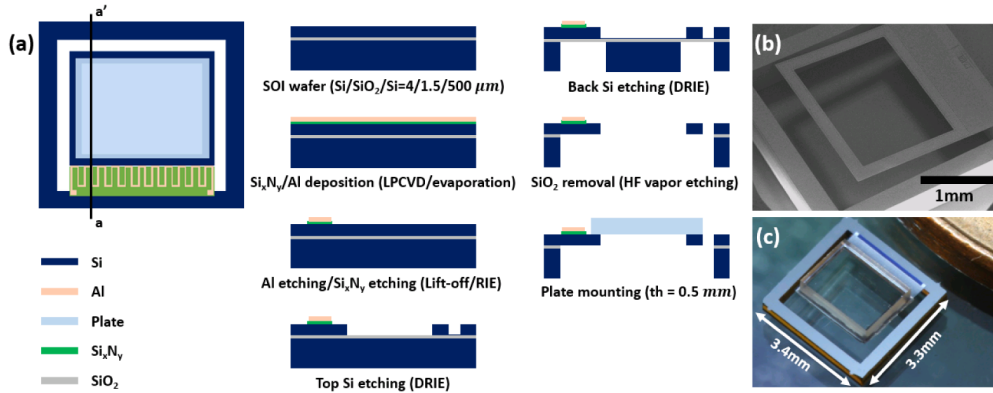

Fig. 2. (a) Microfabrication procedure of the electrothermal microactuator depicted as the cross-section schematics along the line a-a′. (b) SEM image of the fabricated microactuator. (c) Optical image of the MEMS PPR device with anti-reflective glass plate.

4. Experimental results

The mechanical rotation of an optical plate can be statically or dynamically controlled during the electrothermal operation. In this experiment, the microactuator was initially operated without an optical plate by applying different DC bias voltages. The rotation angle was obtained by trigonometric calculation using the vertical displacement values of the silicon frame, measured by the optical microscope. Figure 3(a) shows the rotational angle increases up to 4.75° in static mode with an applied DC bias voltage (15 V$_{DC}$). The experimental results show the small variation in rotational angle less than 0.16° for N = 5 measurements, which corresponds to 0.47 μm in baseline difference. Note that this value smaller than a single pixel size does not significantly affect the image quality. Figure 3(b) clearly indicates the resonant motion of the electrothermal actuator at 840 Hz, which becomes shifted to 136 Hz using sinusoidal wave with offset voltage to confirm precise resonant frequency after the integration of an optical plate due to the inertia of a glass plate. The rotation angle can be precisely controlled by adjusting frequency in different voltage. Finally, the optical plate was resonantly rotated by the electrothermal operation under an applied sinusoidal voltage of 14.4V$_{pp}$ and the optical images were also captured by using the high speed camera

(FASTCAM Mini UX100, 10 μm single pixel size, 1280 x 1024 pixels to 4000 fps) to measure the maximum rotating angle. Figure 3(c) demonstrates the maximum rotating angle of 37° was measured with the overlapped image. To correspond the baseline distance with the designed value, the MEMS PPR device was operated with 14 V_{pp} at resonance frequency to have a rotating angle close to 30° and baseline distance of 100 μm.
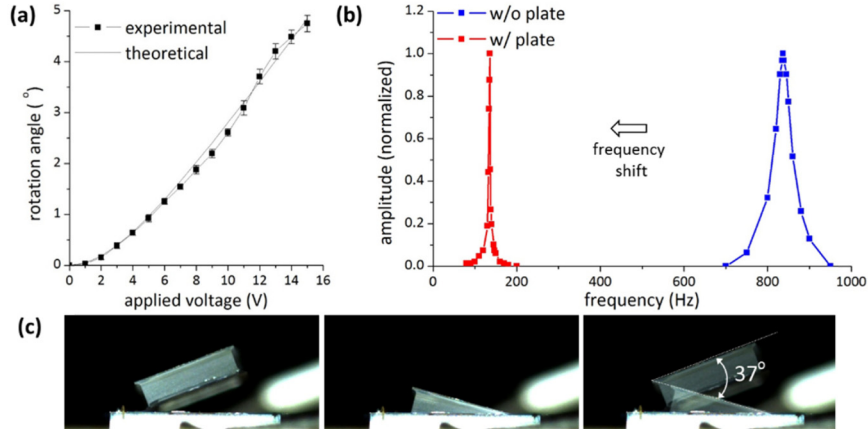

Fig. 3. (a) Mechanical rotation angle of the bimorph plate depending on the applied voltage in static mode. (b) Resonant frequency shift after the optical plate mount. (c) Snapshot of electrothermal actuation with the rotational angle of 37 degree at 14.4 V_{pp} with resonance frequency (see Visualization 1).

The binocular disparities were also experimentally characterized with the MEMS PPR device. A checker board pattern was used to capture stereoscopic images with different object distances as shown in Fig. 4(a). The camera focal length was calculated to be 84 mm for the reconstruction of the depth maps from the disparity maps. Based on a non-local cost aggregation method [18], the binocular disparities were calculated from the stereo image pairs captured by using the MEMS PPR device based stereoscopic imaging system with different object distance. The spatial resolution of stereo-matching algorithms depends on the number of the detectable features over a surface. In order to achieve the binocular disparity from sparse features, a depth approximation method was incorporated by combining the segmentation and non-local cost aggregation [19]. A mean-shift-based segmentation method was firstly applied to subdivide the stereo pair into multiple depth patches. In parallel, a sparse disparity map was computed from the detectable features on the pair by using a non-local cost aggregation method [20]. Finally, the mean disparities of each patch from the sparse disparity map were approximated to yield a complete disparity maps with different distances as shown in Figs. 4(b)-4(d). Note that a close entity was indicated in red and far in blue as shown in Figs. 4(b)-4(d). The disparity values extracted from the disparity maps with different distances were also compared with the theoretical values. Figure 4(e) clearly demonstrates the binocular disparity is inversely proportional to the object distance. Depending on the object distance, the measured disparities indicate that the depth resolution of MEMS PPR is in accordance with normalized theoretical values derived from the inverse-proportional relationship between the binocular disparities and object distances. Note that the object distance over 105 mm exhibits the depth resolution is lower at large distance due to limitation of pixel size.

The representative example for MEMS PPR based stereoscopic imaging successfully demonstrates the anaglyph 3D images and the disparity map in Fig. 4(g) and 4(h), respectively. Both two images were calculated from binocular images by capturing the paper including the word, 'STARWARS'. The anaglyph 3D image was reconstructed by using MATLAB and the disparity map calculated from the stereo image pair of the object with

letters. The disparity map displays gradual decrease of disparity value over distance within a FOV.
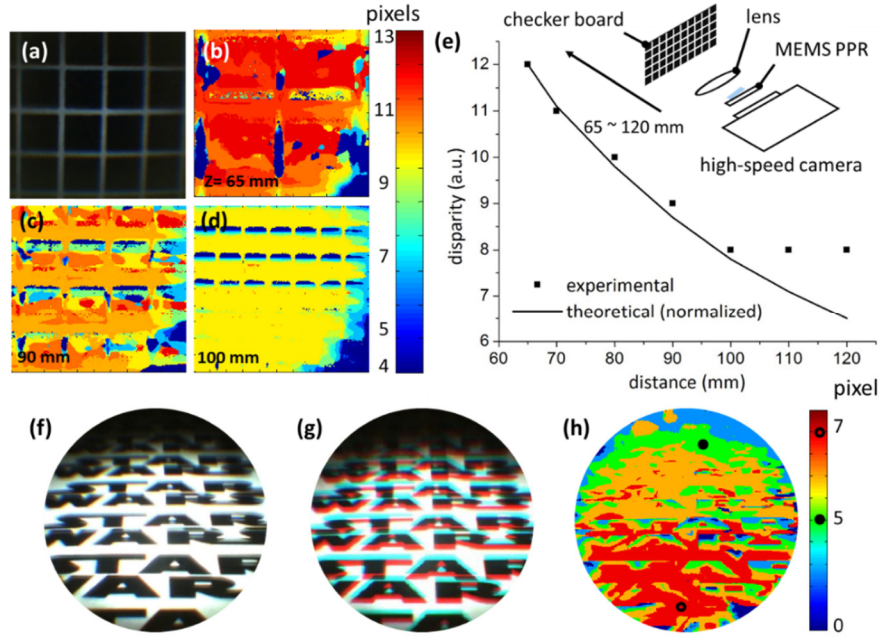

Fig. 4. Stereoscopic imaging with a lens, MEMS PPR and high-speed camera. The rotation axis of the plate is set to be horizontal. (a) Original image at 90 mm, disparity map at (b) 65 mm, (c) 90 mm, (d) 100 mm. (e) Disparities vs. object distance. (f) The paper including the word, 'STARWARS' was reconstructed to (g) anaglyph 3D image and (h) disparity map by binocular images from MEMS PPR. The paper is slightly tilted in front of MEMS PPR therefore the bottom word is close and the top word is far. The relative disparities are scaled in color.

5. Conclusion

In summary, we have successfully demonstrated stereoscopic 3D imaging by employing electrothermal MEMS actuation of parallel-plate-rotation prior to a single camera. The electrothermal actuation under 14 V_{pp} in operating voltage precisely rotates the plate by 30°, which creates binocular disparities comparable to conventional binocular cameras with a baseline distance of 100 μm. The electrothermal actuation allows not only the static rotation of an optical plate but also the resonant motion under low operational voltages. The MEMS PPR has the physical volume of 3.4 mm x 3.3 mm x 1 mm. This work provides a new direction for compact stereoscopic 3D imaging systems such as mobile cameras or stereoscopic endoscopes.

Acknowledgments